AIChE

Analysis of the Effect of Mixing Vane Geometry on the Flow in an Annular Centrifugal Contactor

Kent E. Wardle, Todd R. Allen, and Mark H. Anderson
Dept. of Engineering Physics, University of Wisconsin-Madison, Madison, WI 53706

Ross E. Swaney
Dept. of Chemical and Biological Engineering, University of Wisconsin-Madison, Madison, WI 53706

DOI 10.1002/aic.11855
Published online July 16, 2009 in Wiley InterScience (www.interscience.wiley.com).

The annular centrifugal contactor is a compact mixer/centrifuge developed for solvent extraction processes for recycling used nuclear fuel. This research effort couples computational fluid dynamics (CFD) modeling with a variety of experimental observations to provide a valid detailed analysis of the flow within the centrifugal contactor. CFD modeling of the free surface flow in the annular mixing zone using the volume-of-fluid method combined with large eddy simulation of turbulence was found to have very good agreement with the experimental measurements. A detailed comparative analysis of the flow and mixing with different housing vane geometries (four straight vanes, eight straight vanes, and curved vanes) was performed. Two additional variations on the eight straight vane geometry were also simulated. This analysis determined that at the simulated moderate flow rate the four straight mixing vane geometry has greater mixing and fluid residence time as compared to the other mixing vane configurations. © 2009 American Institute of Chemical Engineers *AIChE J,* 55: 2244–2259, 2009
Keywords: liquid–liquid extraction, reprocessing, turbulent mixing, computational fluid dynamics, volume-of-fluid

Introduction

The annular centrifugal contactor is a unique piece of mixing equipment that has been developed for solvent extraction processes for recycling used nuclear reactor fuel.[1] Solvent extraction consists of thorough mixing of two immiscible fluids and subsequent phase separation with the purpose of achieving extraction of a desired species from one phase to the other. Compared to other available solvent extraction equipment, the centrifugal contactor facilitates process intensification[2] by combining both the mixing and separation functions into a single compact piece of equipment. A sketch of a general centrifugal contactor is shown in Figure 1. During solvent extraction operation, flows of the two immiscible liquids enter the narrow annular region where they are mixed by shear induced by the spinning rotor. The fluid is directed to the rotor inlet by stationary radial vanes attached to the housing below the rotor. Once inside the rotor the two fluids are separated by centrifugation and flow upward and over their respective weirs.

This research effort has focused on providing a more complete understanding of the fluid flow within these contactors to enable further advancements in design and operation of future units and greater confidence for use of such contactors in a variety of other solvent extraction applications. Simulations of the free surface flow in the annular mixing region have been reported previously and it was found that there is discontinuous contact—both spatially and temporally—between the fluid and the rotor.[4] This earlier study looked only at the flow in a contactor with four straight mixing vanes. While various researchers have noted that the flow in the annular mixing region is clearly dependent on the housing vane configuration,[3,5,6] to the authors' knowledge there has not been a detailed comparative study of various mixing

Correspondence concerning this article should be addressed to K. E. Wardle at kwardle@anl.gov

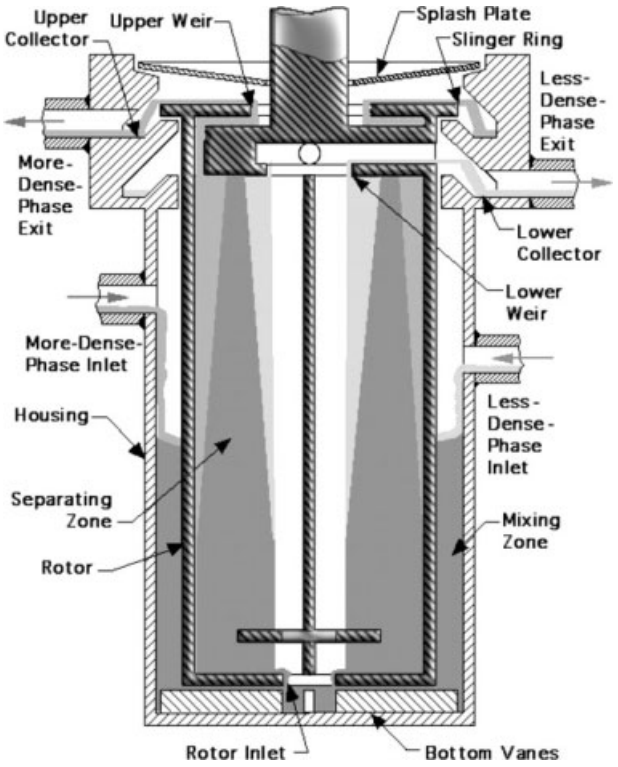

Figure 1. Sketch of the cross-section of an annular centrifugal contactor.

Figure modified from Leonard et al.[3]

vane geometries. Straight housing vanes have typically been used for solvent extraction operation; however, commercially available centrifugal "separator" units manufactured by Costner Industry Nevada Corporation (CINC) use curved housing vanes. It is vital to understand how this design modification affects the operation of the contactor, especially as these commercial "separator" units have been evaluated for use in a variety of solvent extraction applications.[3,5–9] At least one such research effort has noted that the curved vanes seem to result in poorer overall stage efficiency at low flow rates as compared to standard straight vanes.[5,6]

Computational fluid dynamics (CFD) is a valuable tool for analysis of flow and mixing in the contactor and has been used here to enable detailed quantitative comparison between several housing vane geometries. This current study builds upon the previous work which demonstrated the accuracy of CFD simulation using the volume of fluid (VOF) volume tracking method along with large eddy simulation (LES) of turbulence for modeling the single liquid, hydraulic operation of the annular centrifugal contactor.[4] A detailed analysis including both experiments and simulations of the flow in each of three standard vane geometries—four straight vanes, eight straight vanes, and eight curved vanes—is presented here. Additionally, a similar computational analysis for a couple of variations on the 8-vane geometry was conducted and the overall results of those simulations are also included here for comparison. Along with providing an analysis of the flow for different vane geometries, the current work also provides a further validation of the previous methods through the use of more refined mesh simulations made possible through computation resource allocations at the National Center for Supercomputing Applications. To this end, quantitative comparison between simulations and experimental measurements using laser Doppler velocimetry (LDV) and particle image velocimetry (PIV) are given for the 4-vane geometry.

In general, it is assumed here that the simulation scheme—which was shown in the previous work to be valid for the 4-vane geometry[4] and is further compared with experiments here—is equally valid for these other vane configurations. Where possible, comparisons with experimental observations were made for the other vanes to provide support for this assumption. Experiments and simulations at 600 ml/min and 377 rad/s (3600 rpm) in a 5-cm annular centrifugal contactor are described here. Experimental observations of the flow in the mixing zone for the different vane geometries at different flow rates and rotor speeds are reported elsewhere (Wardle et al., submitted).

Droplet breakup and the role of turbulent energy dissipation

Fluid mixing is a critical part of nearly all chemical and engineering processes and has been the subject of significant research over many years and is still an important topic today.[10] In regards to liquid–liquid mixing in centrifugal contactors, understanding the forces which govern the breakup and dispersion of droplets is a key in predicting overall operational efficiency based on the droplet size distributions, interfacial area for mass transfer, and mass transfer rates. The role of energy dissipation in mixing and the formation and distribution of droplets will be reviewed here. While much of the previous research has focused on impeller mixing in stirred tanks, the physical principles are equally applicable to liquid–liquid mixing in centrifugal contactors.

Many theories regarding droplet breakup in liquid–liquid dispersions have been based on the early theories and studies of Kolmogorov and Hinze. Hinze argued that droplet breakup occurs when the relative magnitude of the forces acting to deform a droplet (or bubble) exceed the restoring forces.[11] Restoring forces include interfacial tension (σ) and internal viscous stresses. Internal viscous stresses are important primarily for small liquid droplets with high viscosity. The main deforming forces are the turbulent stresses which are comprised of the viscous shear stress (τ) and turbulent pressure fluctuations. These deforming forces are the product of turbulent eddies with a characteristic length scale of the same order or smaller than the droplet size; it is generally assumed that eddies larger than a droplet cause bulk motion of the droplet rather than its distortion.[12] Hinze suggested that the deformation of fluid particles (droplets or bubbles) could be described by two dimensionless groups representing these two forces affecting droplet stability.[11] These are the Weber number *We* (ratio of inertial forces and interfacial tension) and the viscosity group *Vi* (also called the Ohnesorge number *Oh*) and are defined as:

$$We = \frac{\tau d}{\sigma} \tag{1}$$

$$Vi = \frac{\mu_d}{\sqrt{\rho_d d\sigma}} \quad (2)$$

where d is the droplet diameter, and μ_d and ρ_d are the dispersed phase viscosity and density (denoted by the subscript d). At some critical value of the Weber number We_{crit} where the distorting forces exceed the restoring forces, droplet breakup occurs. Hinze proposed that the overall deformation process could be described by:*

$$We_{crit} = c_1[1 + f(Vi)] \quad (3)$$

For droplet deformation dominated by dynamic local pressure fluctuations, the corresponding stress generated by eddies in the continuous phase (denoted by subscript c) with a length scale λ is given by:

$$\tau \propto \rho_c \overline{u_\lambda'^2}/2 \quad (4)$$

For homogeneous, isotropic turbulence in the inertial subrange, the fluctuating component of velocity $\overline{u_\lambda'^2}$ (where $u = \overline{u} + u'$) is proportional to the turbulent energy dissipation rate ε as:

$$\overline{u_\lambda'^2} = c_2(\varepsilon\lambda)^{2/3} \approx 2.0(\varepsilon\lambda)^{2/3} \quad (5)$$

Assuming that the characteristic eddy length scale of interest $\lambda \gg d_{max}$, that is, deformation of droplets are caused primarily by the dynamic pressure fluctuations of eddies with a similar size, We_{crit} can be written as:

$$We_{crit} = \frac{\rho_c \varepsilon^{2/3} d_{max}^{5/3}}{\sigma} \quad (6)$$

For the case of $Vi \gg 1$ (negligible internal viscous stresses) the maximum stable droplet diameter is then given by:

$$d_{max} = c_3 \left(\frac{\sigma}{\rho_c}\right)^{3/5} \varepsilon^{-2/5} \quad (7)$$

Haas[13,14] experimentally determined the value of c_3 in Eq. 7 to be $c_3 = 1.2$ for data from three different liquid–liquid mixing devices (including an annular mixer) along with data from Davies.[15] There was agreement for a wide range ($\sim 10^4$) of energy dissipation rates. It is clear from Eq. 7 that the continuous phase turbulence dissipation rate ε can be directly related to the degree of liquid–liquid mixing. For given fluid properties, as the dissipation rate increases, the maximum stable droplet size decreases. As a result, it is common for numerical studies of mixing to calculate only the flow patterns for single-phase flow in mixing devices and to infer from this the liquid–liquid mixing behavior based on the predicted turbulent energy dissipation rate. For simulations of the centrifugal contactor as presented here, it is thus possible to make direct comparison between the predicted turbulent energy dissipation for the various vane systems as an indicator of the mixing efficiency for these different geometries.

*Note that throughout this section and the following sections, generic empirical constants will be numbered c_1, c_2, c_3,... and so on to avoid confusion.

Spatial distribution of energy dissipation

Energy dissipation in typical mixing vessels is inhomogeneously distributed. For example, in stirred mixing vessels the energy dissipation in the impeller region can be $\sim$100 times the average ($\varepsilon/\bar{\varepsilon} \sim 100$).[16] While the average power dissipated per unit mass ($\bar{\varepsilon} = P/\rho V$ where P is power and V is volume) is often used to characterize a given mixer and for device scaling, it is the local dissipation, specifically the maximum dissipation rate ε_{max}, which has been shown to be the dominant factor for mixing.[16–19] The effect of the main flow field is also important to the overall mixing in determining the amount of time that the fluid spends in the regions of high dissipation. For the centrifugal contactor, the highest liquid shear occurs when the fluid is in contact with the rotor and, therefore, an evaluation of mixing must take into account not only the magnitude of the dissipation rate for the liquid near the rotor but also the dynamic fluid-rotor contact area.

Methods

Experimental setup

The contactor apparatus that was used for the experimental observations presented here was described previously[4] and consisted of a 5-cm centrifugal contactor manufactured by CINC Industries (model V2). Three different mixing vane geometries were available for this apparatus: four straight vanes (4-vane), eight straight vanes (8-vane), and eight curved vanes (curved). The curved vane configuration is unique to CINC manufactured separator units and will be described in detail later. The housing of this contactor unit was modified to have a quartz cylinder to facilitate optical measurements.

Experimental measurements of velocity using the LDV and PIV techniques were performed for the 4-vane geometry. The setup for these measurements is described in detail elsewhere.[4] The LDV and PIV measurements were both made without artificial seeding by using as light scattering particles the entrained air bubbles that are unavoidable due to the violent mixing and free surface flow in the centrifugal contactor. Wardle et al.[4] explored the effect of bubble size on the accuracy of these measurements and found that the measured velocities were not strongly affected by a change in average bubble size achieved through the addition of a surfactant. LDV data were obtained across the annular mixing zone at four different axial heights. PIV data were taken on a plane that was oriented tangentially to the rotor. Because of curvature effects of the housing cylinder, only PIV data along the vertical centerline (even with the axis of the rotor) are presented here for quantitative comparison with simulation. High-speed video imaging was conducted to observe the flow in the annulus for each of the three vane geometries. This also enabled comparison of the actual and predicted annular liquid heights (ALHs) for each case.

Computational methods

The general modeling scheme for these simulations was based on the VOF/LES simulations presented by Wardle

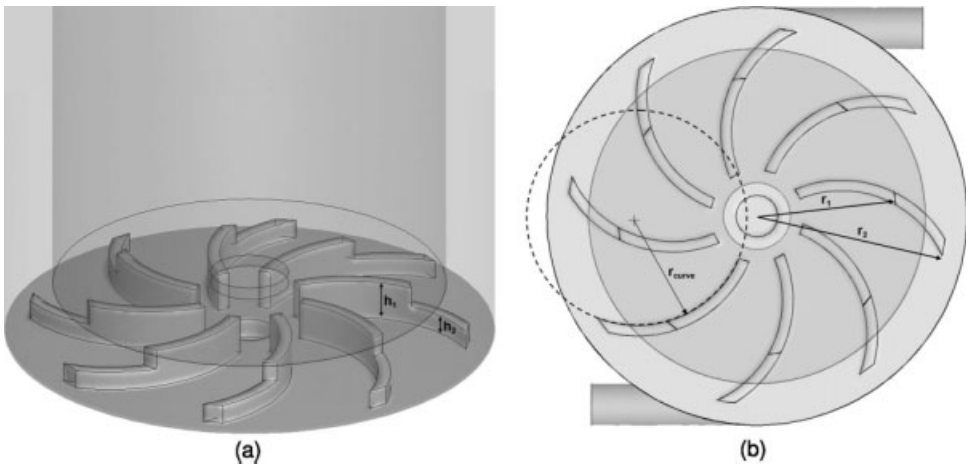

Figure 2. Curved vane contactor model with geometric parameters labeled (see Table 1 for values).

et al.[4] However, a few key changes that were made to the CFD model setup are explained here.

The CFD simulations were performed using Fluent 6.3. All simulations used the VOF model with piecewise linear interface construction (PLIC) and the LES technique for simulation of turbulence using a dynamic, one-equation turbulent kinetic energy transport subgrid model.[20] The combination of these two models as implemented in Fluent uses first-order time discretization. Bounded central differencing was used for spatial discretization of the momentum and subgrid kinetic energy equations to limit numerical diffusion. The subgrid scale dissipation rate was calculated from the local subgrid turbulent kinetic energy as set forth in Kim and Menon.[20] The boundary conditions and set up of the CFD simulations were the same as those used previously (600 ml/min water inlet flow, 377 rad/s rotor speed) except for a few changes. Firstly, the contact angle of the liquid on the solid surfaces of the model was changed to 75° to better account for the actual contact angle of water on steel (the typical material of construction for contactor units); this change had a very minor effect on the overall predictions of the simulations.[21] A second important change in the model configuration, namely, the specification of the pressure distribution on the mixing zone outlet (rotor inlet) is discussed later.

Geometries and meshing

The flow in the mixing zone was analyzed for the three experimentally available vane geometries (4-vane, 8-vane, and curved vane). Additional variations to the standard eight straight vane geometry were also simulated. These were an 8-vane geometry with a vane-wall gap equal to half of the annular gap Δr and one with a modified housing in which the width of the annular gap was decreased such that a radius ratio $r_r/r_h = \eta = 0.9$ was achieved (same rotor radius, $r_r = 2.54$ cm). Regardless of the vane geometry, the vane height h_v for each configuration was 0.515 cm. This was corrected from the previous models to match the experimental setup. Note also that each vane type had a vane thickness of 0.159 cm (1/16″), consistent with the experimental geometry.

The 4-vane geometry used here is identical to that given in Wardle et al. (with the exception of h_v).[4] The 8-vane housing geometry is similar to the four (i.e., same vane dimensions, etc.) except that there are eight housing vanes instead of four. The model curved vane geometry is shown in Figure 2 and the corresponding geometric quantities are listed in Table 1. It can be seen in Figure 2a that the vanes have a two-tiered construction. There is a section of full height (h_1), equivalent to the vane height of the 4- or 8-vane geometries, that extends out to a radius r_1 of 2.1 cm (recall that the rotor radius r_r is 2.54 cm). Beyond this radial distance, the height of the vanes is decreased by about half. Further, the vanes—of which there are eight—do not extend all the way to the housing wall but end at the midpoint of the annular gap. It was shown in simplified models of this geometry[21] that these features allow for a band of steady tangential flow around the outer edge of the bottom of the housing and the stepped feature also generates some slight upward flow.

Access to additional computational resources through a National Science Foundation TeraGrid grant (TG-ECS070009) enabled these simulations to be conducted at a higher level of grid refinement than those in the previous work.[4] Specifically, it was possible to increase the node density by a factor of nearly 3 compared to the earlier simulations that were performed on a local Linux cluster; all the meshes used for the various geometries presented here had ~800 K tetrahedral computational cells. The grid points were refined within critical regions of the flow (i.e., the lower portion of the side of the rotor, the bottom of the rotor, and the narrow gap between the vanes and the rotor bottom); for each case, the smallest cells had dimensions of 0.05 cm and the largest 0.1 cm. Table 2 lists the total number of computational cells for the various models. Despite

Table 1. Selected Geometric Parameters of Curved Vane Contactor Mixing Zone Model Shown in Figure 2

Vane Parameter	Symbol	Value (cm)
Full height	h_1	0.515
Stepped height	h_2	0.248
Radius of curvature	r_{curve}	2.855
Radius (full height)	r_1	2.100
Radius (total)	r_2	2.855

Values not listed are the same as the 4-vane geometry given in Wardle et al., 2008.[4] The vane thickness is 0.159 cm (1/16″).

Table 2. Number of Computational Cells for the Models of the Various Mixing Vane Geometries

Vane Geometry	N Cells (K)
4-Vane	797
8-Vane	829
Curved	776
8-Vane, vane-wall gap	858
8-Vane, $\eta = 0.9$	829

the increased grid density used here as compared to the previous work, due to the high Reynolds number (~60,000 at typical conditions in this device) and high computational cost of the transient VOF simulations, these are as yet relatively "coarse" meshes for LES; the grid spacing near the rotor is estimated to be about an order of magnitude greater than the Taylor microscale in this region and wall functions are used in this study as in the previous work.[4] The time step was allowed to vary to maintain a global Courant flow number Cr of 2.0; for these simulations the typical time step was ~15 μs. The 4-vane and curved vane simulations were performed in parallel on 40 processors (3.2 MHz) and the 8-vane simulations were done on 44 processors. In general, it was found that a distribution of ~20,000–25,000 cells per processor was near the speed-up threshold. Similar to the previous simulations, the required computation time was ~80–100 h per 1 s of flow time.

Modification of outlet boundary condition

As described in the previous work,[4] the use of two separate pressure boundaries (one on the top annular surface and one at the rotor inlet) enabled prediction of the liquid hold-up in the mixing zone. The simulations presented in the previous work applied a spatially (and temporally) constant pressure boundary condition of −53.6 Pa on the mixing zone outlet. This was the value computed using the Bernoulli equation for rotating flow if one assumes the negative pressure at the rotor inlet is generated by the rotating column of air within the rotor (see Figure 1) and sets the outer radius of the light phase outlet equal to the rotor radius (2.54 cm). However, the actual radius of the light phase outlet for the rotor of the CINC V-2 contactor which was used for the experiments is 3.15 cm (unlike the sketch in Figure 1, the radius of the upper section of the CINC V-2 rotor is greater than that of the main section[22]). Using this value, the calculated pressure from the Bernoulli equation (for a rotation rate of 377 rad/s) is −83.3 Pa relative to atmospheric pressure. It was verified with actual measurements of the pressure that this is indeed an accurate value of the static pressure at the center point of the rotor inlet for the 4-vane geometry. Initially, simulation of the 4-vane geometry (using the refined meshing outlined in the previous section) was performed using a radially uniform −80.0 Pa outlet pressure. While it was found that the predicted average minimum ALH decreased from the −53.6 Pa outlet case by about 2 mm, this was still ~12 mm higher than the experimentally observed value. Based simply on a hydrostatic balance of liquid heights, a 12 mm difference in liquid height (of water) corresponds to a decrease of ~120 Pa; thus, it was determined that the average pressure of the rotor inlet boundary must actually be −200 Pa in order for the simulation to match experiment.

As it was established from the experimental measurements that the pressure at the center point of this surface is −80 Pa, it was assumed that there could be a pressure profile across the inlet surface such that the pressure is indeed −80 Pa at the center but decreases radially such that the average pressure of the surface equals −200 Pa. Further, a profile of this nature has a reasonable physical explanation. It was observed from previous mixing zone simulations that the majority of the flow enters the rotor near the outer edge of the rotor inlet surface. This flow tendency is also likely enhanced in reality because the rotor inlet acts as a weir such that fluid entering the rotor is quickly spun out toward the outer wall of the hollow rotor. This is true of a "fully-pumping" rotor in which the liquid/air free surface within the rotor has a radial position greater than the radius of the rotor inlet (by design) in order to help pump fluid into the rotor. It has been observed experimentally that increasing the radius of the rotor inlet increases the height of liquid in the annular region.[5] This likely occurs due to a decrease in the magnitude of negative pressure at the rotor inlet and a flattening of the radial pressure profile.

For the simulations presented here, a parabolic pressure profile $P(r)$ of the form:

$$\begin{aligned} P(r) &= C_0 + C_1 \cdot r^2 \\ C_0 &= -80 \text{ Pa} \\ C_1 &= -1.44 \times 10^7 \text{ Pa/m}^2 \end{aligned} \tag{8}$$

was applied to the mixing zone outlet pressure boundary. A parabolic profile was chosen as this is the form for static pressure head in "rigid" rotation. The coefficients C_0 and C_1 were determined such that the pressure at the center point ($r = 0$) is −80 Pa and the average pressure obtained by integrating over the entire surface is −200 Pa. For this profile, the minimum pressure of −448 Pa occurs just at the outer edge of the rotor inlet ($r = 0.505$ cm).

Measurements of the pressure at the center point of the rotor inlet identified differences in behavior for the three different vane geometries. For example, the curved vane geometry exhibited a slight positive deviation (~30 Pa) from the Bernoulli equation predicted value. However, lacking a better, more generalizable method for specifying this boundary condition across a variety of vane geometries, it was chosen to apply the same rotor inlet boundary pressure profile given in Eq. 8 to the simulations of each of the various vane geometries. Comparison of the results of these simulations with experimental observations for the 8-vane and curved vane configurations will help in understanding the impact of this approximation for these cases. Note, however, that it was seen previously from a 4-vane case in which the radially uniform pressure setting was changed from −53.6 to −80.0 Pa—a difference approximately equal to the difference between the measured pressure of the 4-vane and the curved vane geometries for the given conditions—that the effect on the overall ALH was minimal (~2 mm decrease in average ALH) although there was a noticeable decrease in liquid hold-up volume (~15%). As will be shown by the results of the simulations, the differences in mixing behavior for the

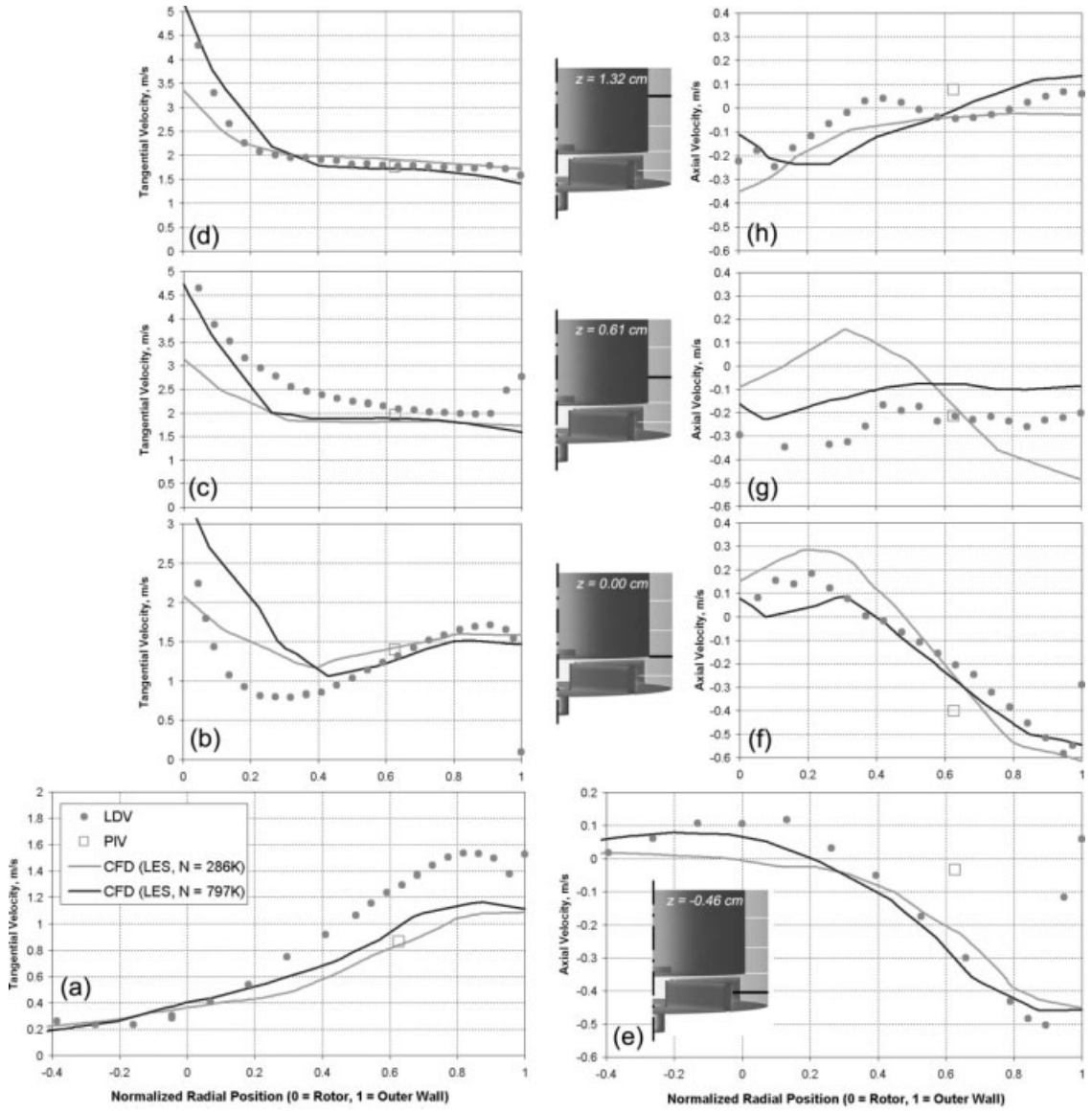

Figure 3. Plots of the LDV measured mean velocities for the 4-vane geometry at the four different axial positions (relative location noted by inset images) as compared to the current CFD simulation predictions (N = 797 K) and those from Wardle et al. (N = 286 K).[4]

The radial position has been normalized by the annular gap width Δr.

various vane configurations are much more than 15% and therefore the observed trends are considered valid despite this potential uncertainty due to the outlet pressure specification. Further, comparison with experimental observations for flow in the different vane configurations provides a separate means of validating this assumption.

Results and Discussion

Comparison with experimental velocity measurements

The main purpose of the simulations in the previous work[4] were to demonstrate the validity of the computational modeling scheme and aid in the selection of the most appropriate turbulence modeling method through direct comparison with experimental data. To demonstrate the improved accuracy of these more refined-grid simulations, comparison with previous LDV measurements and simulations (using LES) are shown here. Additionally, quantitative comparison with experimentally measured velocity profiles from PIV is also given. Again, the standard operating conditions of 600 ml/min and 377 rad/s (3600 RPM) are used. The equilibrated simulations were averaged over 1 s of flow time.

Comparison with LDV Data and Previous Simulation. Figures 3 and 4 give plots of the average and RMS velocity profiles in the annular region as obtained from the current simulations compared with the experimental data reported previously in Wardle et al.[4] The profiles obtained from the LES simulations of the 4-vane geometry presented in the previous chapter are also included for comparison. It is

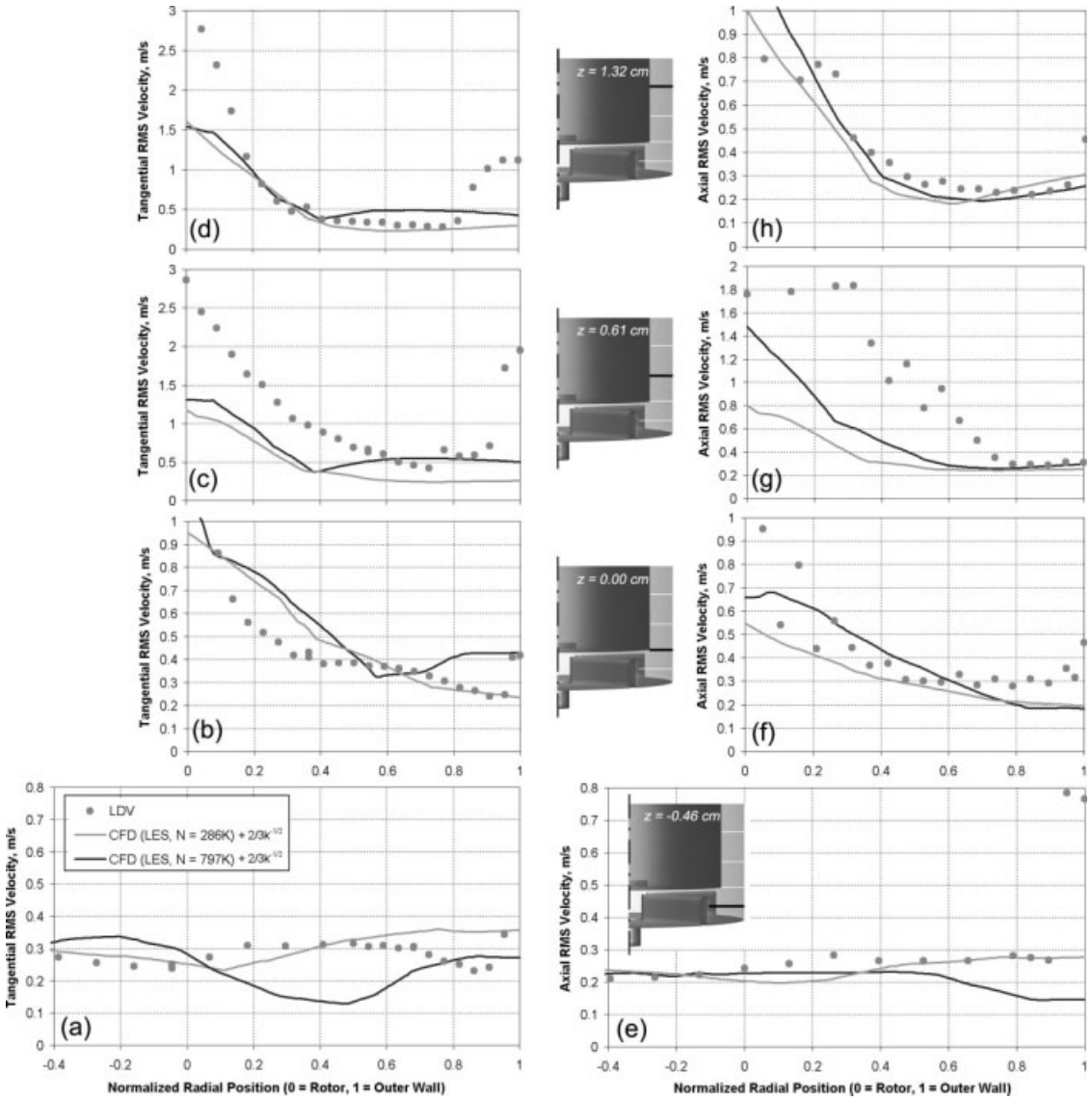

Figure 4. LDV-measured and CFD-computed RMS velocity profiles for the 4-vane geometry at the four different axial positions (location noted on inset images).

The RMS values from CFD include both the calculated time variation and the contribution from the subgrid turbulent kinetic energy k.

evident that there is an improvement in the accuracy of the current CFD simulations with more refined meshing. Ideally, one would like to refine the mesh as much as necessary to achieve a grid independent solution; however, the VOF model is inherently grid-dependent and full resolution is not feasible for the given computational problem due to the violent free surface motion and bubbly flow within the mixing zone of the contactor. Consequently, the improved accuracy shown here is not unexpected. In particular, the slope of the tangential velocity near the rotor is more accurately captured with the current simulations. Also, it can be seen that there is improvement in the predictions of the flow at the $z = 0.61$ cm height, particularly for the axial velocity. This improvement is primarily due to more accurate prediction of the absolute magnitude of the ALH due to the modified outlet pressure profile. In Figure 3g it can be seen that the height of the lower Taylor-Couette cell (denoted by upward flow near rotor in Figure 3f) is better predicted and there is downward flow near the rotor in this simulation at the $z = 0.61$ cm height.

The ALH predictions for the various geometries are compared later (see Table 3). For the 4-vane geometry, a significant improvement in the predicted liquid height oscillation frequency was also observed with the current simulations. An average oscillation frequency of 4.74 ± 0.9 Hz was predicted from these simulations which is very close to the value of 4.75 ± 0.16 Hz obtained from LDV measurements as reported in the previous work.[4]

Comparison with PIV Data. PIV of the flow in the annulus of the 4-vane geometry was performed at various flow rates and rotor speeds as reported elsewhere.[21] Data was taken for the flow in a vertical laser sheet in the annular

Table 3. Comparison of Experimentally Observed and Simulation Predicted Annular Liquid Heights Above Rotor Bottom (at 3600 rpm and 600 ml/min)

	Experiment		Simulation	
Vane Type	ALH min (cm)	ALH max (cm)	ALH min (cm)	ALH max (cm)
4-Vane	3.50 ± 0.34	5.28 ± 0.26	3.23 ± 0.12	5.41 ± 0.35
8-Vane	1.1	–	0.95 ± 0.08	–
Curved	2.4	3.4	2.00 ± 0.08	3.06 ± 0.12

region and oriented tangential to the rotor. This data provides another method of evaluating the quantitative accuracy of these CFD simulations of the free surface flow in the contactor mixing zone.

A comparison of the mean tangential and axial velocity profiles at 600 ml/min and 377 rad/s for the vertical line even with the rotor axis in the PIV plane are shown in Figures 5a, b, respectively. The agreement between the experimental data and simulation predictions for the tangential velocity is remarkably good (Figure 5a). The maximum tangential velocity has a very comparable magnitude though it occurs at a slightly lower axial height. Such is also the case for the axial velocities (Figure 5b)—the magnitude of the maximum value is comparable but occurs at a somewhat lower height than the measured profile. The experiment exhibited a maximum downward flow velocity at ~0.25 cm above the rotor bottom whereas the CFD-predicted value occurs at 0.25 cm below the rotor bottom. Note that it was seen in Figures 3f, e that there is a similar discrepancy between the PIV and LDV measured velocities with the simulation predictions falling closer to the LDV measured values. The reason for the discrepancy in this region is unclear but may be related to the characteristics of the air bubbles and their independent influence on the two measurement techniques or may simply be evidence of a limitation of the simulations in this region. In general, the comparison is reasonably good and together with the LDV data and the various observations presented in the following two sections provides further confidence in the quantitative utility of these CFD simulations of the free surface flow using VOF with LES turbulence simulation.

Flow in the annular region

Figure 6 shows time-averaged images obtained from high-speed video of the flow at 600 ml/min (300 ml/min in each inlet) and 377 rad/s (3600 rpm) as viewed from the side for each of the three cases (flow is from right to left). For these time-averaged images (averaged over 2.5 s), it is possible to get a good overall picture of the flow in the annular region. The differences in average ALH between the three vane types are very apparent; at these conditions, the 4-vane has a higher ALH than the other two configurations.

The computational simulations for each of the three standard vane configurations were able to accurately capture the same trends in ALH as seen from the time-averaged liquid volume fractions on the housing wall shown in Figure 7. The specific values for the CFD-predicted and experimentally observed annular liquid levels are given in Table 3. The ALH was extracted from the simulations in the same manner as done previously[4]—taking an integral of the water volume fraction over the housing wall area, dividing by the circumference of the housing ($2\pi r_h$) and subtracting off the height of the rotor bottom—however, in this case the resulting ALH values were then also corrected to eliminate the spurious ''liquid height'' added by the integrated area of the inlet rivulet running down the housing wall (which for the 8-vane geometry in particular is a significant fraction of the

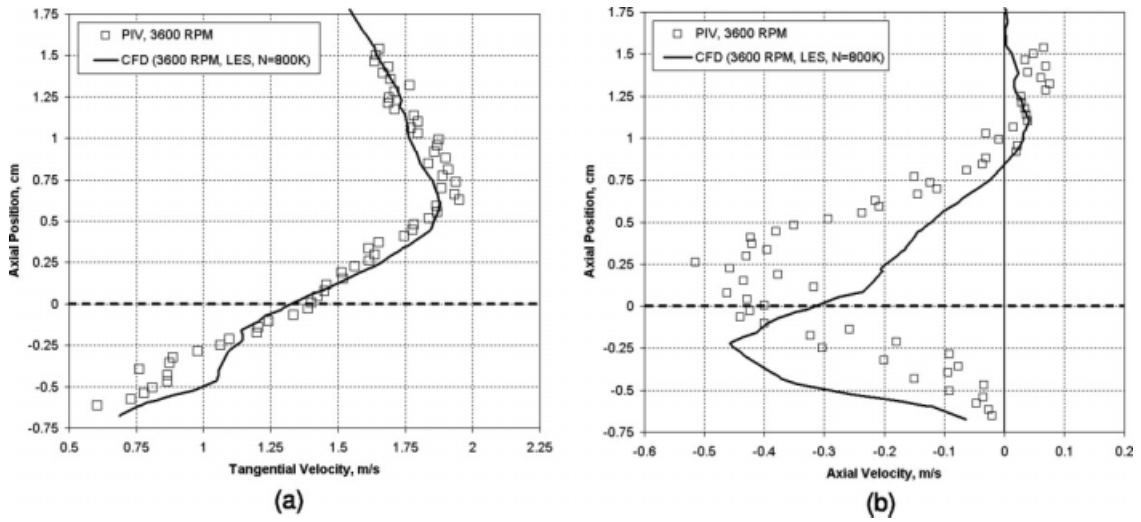

Figure 5. Comparison of PIV data and the current CFD simulation of the 4-vane geometry for the tangential (a) and axial (b) mean velocity along the line even with the rotor axis.

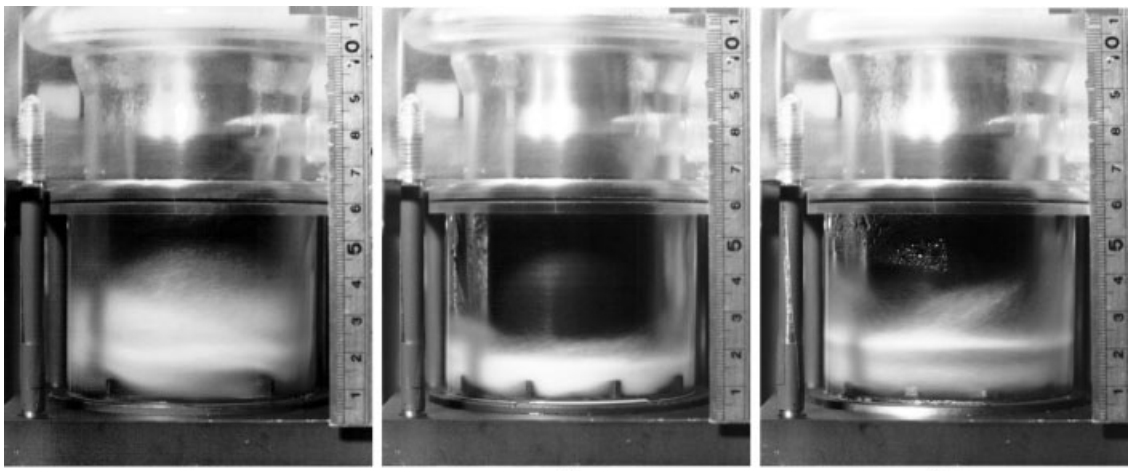

Figure 6. Time-averaged images for the flow in the annular region for the 4-vane (a), 8-vane (b), and curved vane (c) geometries.

Each image is an average of those taken at 100 Hz over 2.5 s of flow time (250 images). The rotor bottom is at ~1.3 cm on the ruler.

real liquid height) to provide a more consistent comparison with experiment and the other vane cases. The experimental ALH measurements given in Table 3 are a visual approximation from direct observations during experimentation as well as postexperimental analysis of high-speed video images. For the 4-vane geometry in particular, a greater number of observations were made as part of several different experimental runs over a range of flow rates and therefore an average value and standard deviation are reported. The 8-vane and curved vane ALH values from experiment are only estimates of the averages as observed from high-speed imaging and a few recorded observations. In general, there is good comparison between the experiments and values predicted from simulation. The liquid height prediction for the curved vane geometry is somewhat lower than the actual value. Experimentally, it was observed that the curved vane (and 8-vane) geometry experiences a flow transition where at low flow rates the flow has a higher liquid height but appears to be characterized by very little fluid-rotor contact and large voids (this is described more in Wardle et al., submitted). It appears that the mixing zone flow structure predicted from the simulation of the curved vane case is more consistent with the "collapsed" flow type that occurs experimentally at slightly higher flow rates. This may be due to the outlet boundary pressure specification being slightly too negative.

The real power of the computational models is in providing a means for complete visualization of the interior of the flow enabling a comparison of the fluid-rotor contact for the various vanes. Figure 8 shows plots of the time-averaged water volume fractions on the rotor side and a vertical cross-sectional plane (instantaneous snapshots are shown later in Figure 12). It is clear that the amount of fluid-rotor contact is significantly higher for the 4-vane case than either of the other two. There is a region near the bottom of the rotor where the contact is consistently high and above this there are bands where there is fluid-rotor contact as much as 30%

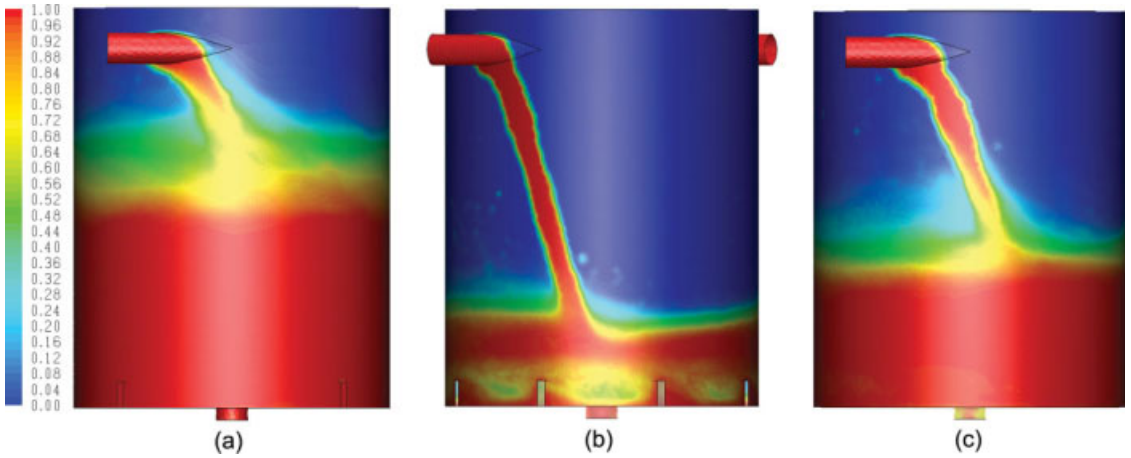

Figure 7. Time-averaged water volume fractions in the annular region from CFD for the 4-vane (a), 8-vane (b), and curved vane (c) geometries.

[Color figure can be viewed in the online issue, which is available at www.interscience.wiley.com.]

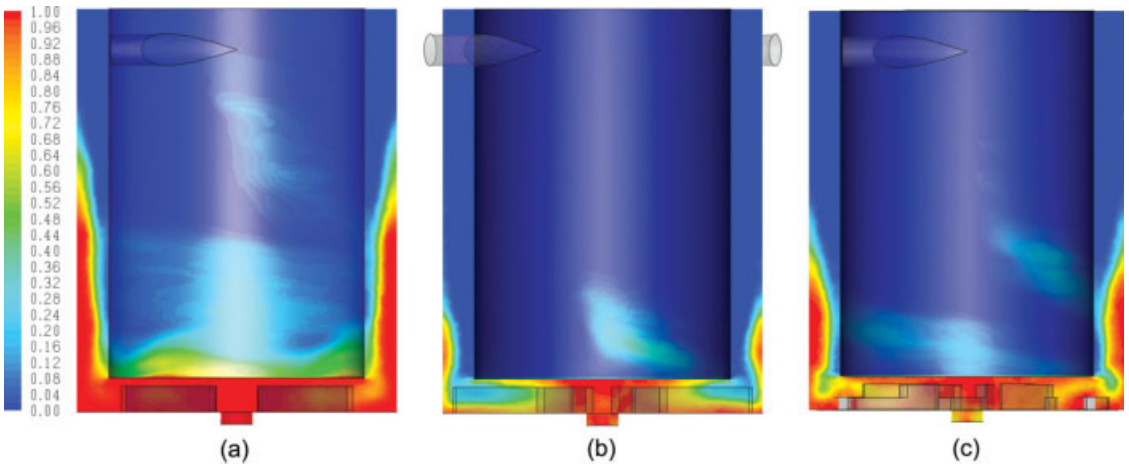

Figure 8. Time-averaged water volume fractions on the rotor side and a vertical annular cross-section from CFD for the 4-vane (a), 8-vane (b), and curved vane (c) geometries.

[Color figure can be viewed in the online issue, which is available at www.interscience.wiley.com.]

of the time. This is consistent with the previous simulation results.[4] For the 8-vane geometry (Figure 8b), there is very little contact between the fluid and the side of the rotor. Further, the volume of liquid in the mixing zone is significantly less and there are large air voids near the lower outer edge of the rotor as well as air being pulled under the rotor. Similar but less dramatic features are visible for the flow in the curved vane geometry (Figure 8c). Here also, the average fluid contact on the side of the rotor is quite low.

Another critical characteristic of the flow for evaluating operation is the steady-state liquid hold-up volume in the mixing zone. It is clear from the experimental images in Figure 6 that there is a significant difference in liquid volume for the three different cases. This difference is discussed further in the context of the mixing evaluation presented in a later section.

Flow under the rotor

The flow underneath the rotor for the base case conditions will be discussed here. Experimentally, the flow under the rotor was observed using high-speed and PIV imaging as reported elsewhere for both the 4-vane and 8-vane geometries. While the large bubble sizes in this region precluded quantitative use of PIV processed vector fields, this data is still quite informative for providing a qualitative description of the flow field under the rotor. The vector field (and corresponding streamlines) for the 4-vane and 8-vane PIV measurements are shown in Figure 9 (for more details on these measurements see Wardle et al., submitted). For the 4-vane geometry, there is a large central vortex rotating in the clockwise direction (same as rotor rotation) that is shifted slightly off-center in the forward flow direction. For the 8-vane geometry, there is only a very weak general rotation

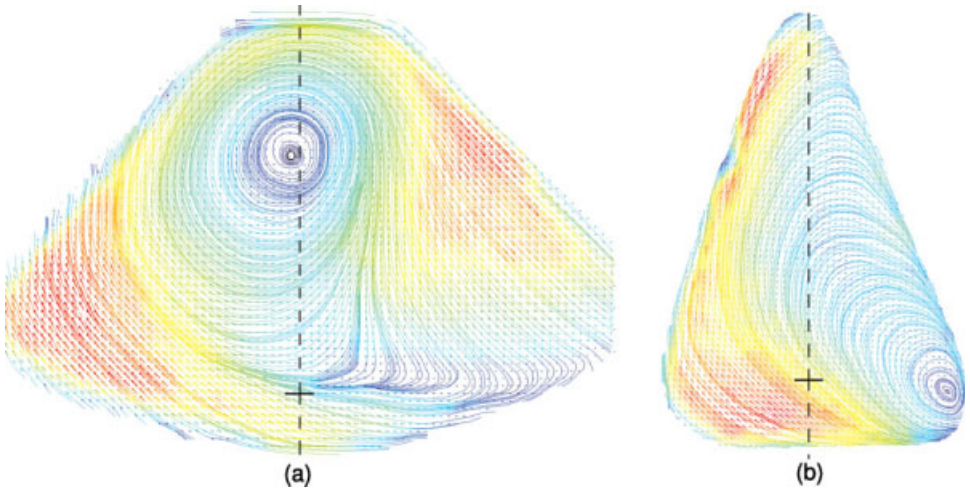

Figure 9. PIV processed vector fields of the flow underneath the rotor at 600 ml/min and 3600 rpm for the 4-vane (a) and 8-vane (b) geometries.

The approximate location of the outer edge of the rotor is marked on the bisecting line (dashed line). For more details on these measurements, see Wardle et al., Experimental study of the hydraulic operation of an annular centrifugal contactor with various mixing vane configurations, submitted. [Color figure can be viewed in the online issue, which is available at www.interscience.wiley.com.]

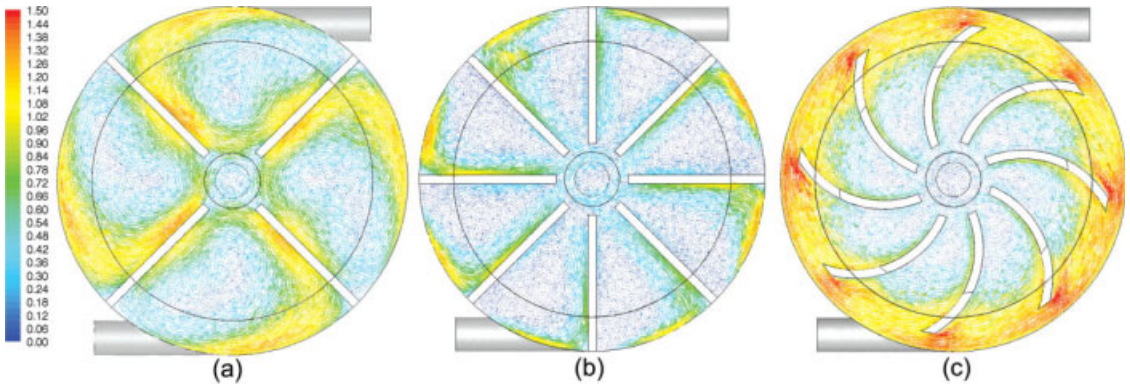

Figure 10. Mean velocity vectors for the flow under the rotor on a horizontal plane located at the mid-vane height from simulations of the 4-vane (a), 8-vane (b), and curved (c) housing geometries.

[Color figure can be viewed in the online issue, which is available at www.interscience.wiley.com.]

and the majority of the flow appears to go radially inward along the forward vane wall toward the axis of the rotor.

The same vector fields predicted by CFD simulation are shown in Figures 10a–c for the 4-vane, 8-vane, and curved vane geometries, respectively. Note that the simulation geometry is a mirror image of the experiment. The predicted flow field in the 4-vane geometry is very consistent with that seen from the PIV imaging as shown in Figure 9a. Again, there is flow in each of the vane regions that is rotating in the direction of rotor rotation (counter-clockwise in the model). The highest magnitudes are in the area of the forward corner of the vane region and flowing radially inward up the forward vane. Experimentally, it was observed that large bubbles tend to form and collect in the center of this large vortex in the vane region. The simulations were also able to capture some large air bubbles underneath the rotor for the 4-vane geometry. These large bubbles appeared to be generated by detachment from the main free surface at the side of the rotor as shown in Figures 11a, b. In general, large bubbles such as this were unstable in the simulations and broke up into many smaller ones soon after their formation; this is consistent with experimental observations at this flow rate.

For the 8-vane geometry (Figure 10b), the overall flow magnitudes in this region are somewhat less than for the 4-vane case. Consistent with Figure 9b, the highest flow magnitudes are at the outer wall and flowing radially inward on the forward vane. Note, however, that the orientation of the vanes relative to the inlet is shifted by 22.5° as compared to the orientation in the experiment. This may have had a slight effect on the predicted flow field as compared to experiment because it is apparent that there is a small degree of asymmetry between the various vane sections with those away from the inlets having slightly higher mean velocities.

The flow under the rotor in the curved vane geometry, for which experimental observation was not possible, is shown in Figure 10c. There is a significant amount of continuous tangential flow near the housing wall due to the gap between the vanes and the wall. There is also a peak in mean velocity just behind the outer edge of the vanes where there is some slight generation of additional turbulence. It appears that the length of the full-height section would likely have an effect on the inward radial flow of the fluid. A longer full-height section would probably result in greater radial pumping; simplified modeling of a curved vane geometry with full height vanes extending all the way to the housing wall was done previously which also demonstrated this (included in Wardle[21]). While such a full curved vane geometry was not simulated with the current free surface modeling methods, it is likely that this system would exhibit very low liquid volumes and poor mixing.

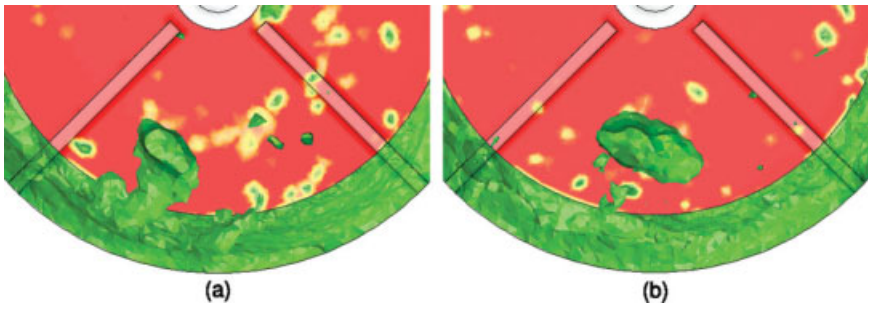

Figure 11. Snapshot of the formation of a large air bubble under the rotor as viewed from below for the 4-vane simulation.

The images are separated by 42 μs. [Color figure can be viewed in the online issue, which is available at www.interscience.wiley.com.]

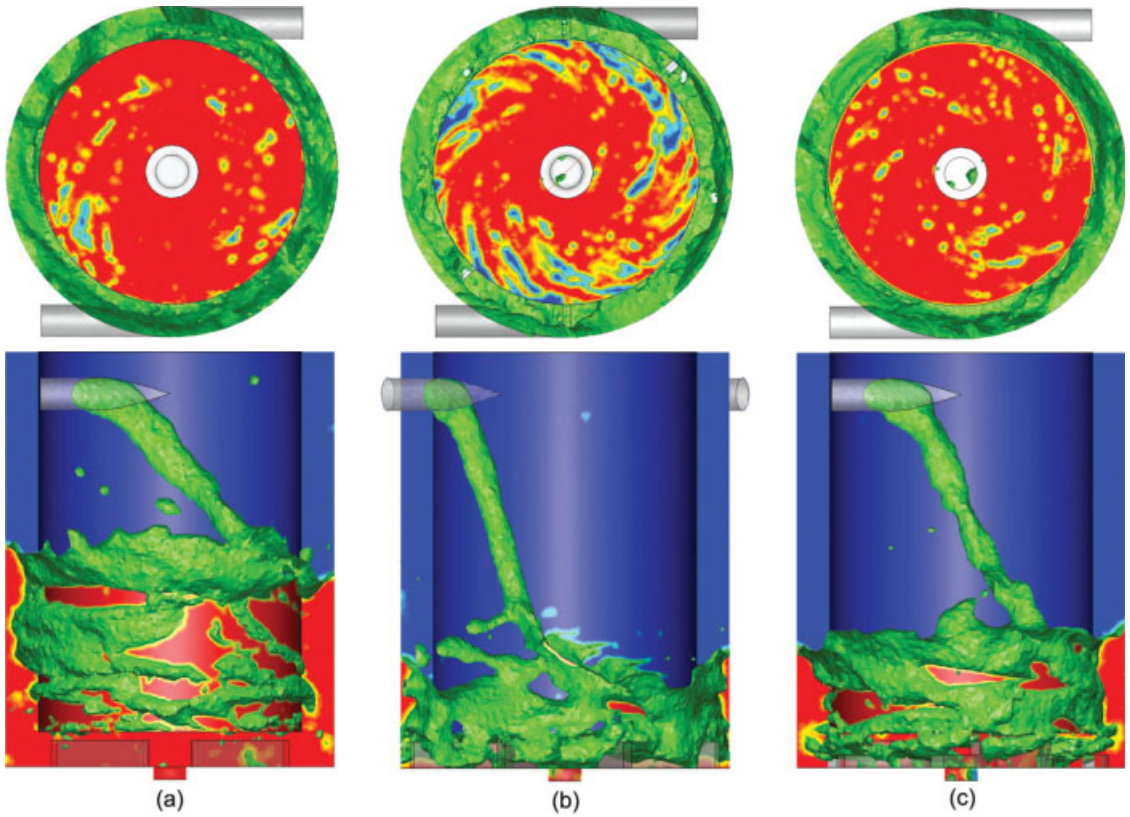

Figure 12. Snapshots of characteristic maximum fluid-rotor contact for the 4-vane (a), 8-vane (b), and curved vane (c) geometries.

The upper image is a view from above showing the contact between the fluid and the bottom of the rotor. [Color figure can be viewed in the online issue, which is available at www.interscience.wiley.com.]

Comparative mixing analysis

A great advantage of these CFD simulations of the flow in the mixing zone of the contactor is their potential for aiding in the evaluation of the mixing behavior for various alternative configurations. While in these simulations the only "mixing" is that between air and water, as was set forth earlier it is also useful to explore the characteristics of the flow of the liquid phase and infer from this the probable liquid–liquid mixing behavior. As outlined in the Introduction, the turbulent energy dissipation rate ε is directly related to the droplet size of a liquid–liquid dispersion and is thus a key metric for understanding and evaluating mixing.

The turbulence dissipation rate is highest at the rotor side where the velocity (and its gradients) is largest. Further, for mixing within the liquid phase, the total area over which this high dissipation rate occurs (the fluid-rotor contact area) also has a substantial impact on how much energy is imparted to the fluid. Also directly related to mixing is the mean fluid residence time which can be estimated as the mean liquid volume divided by the volumetric flow rate. Each of these factors can be predicted from the mixing zone simulations and are discussed here.

As described previously in the context of the time-averaged plots (Figures 7 and 8) of these simulations, there are stark differences between the fluid-rotor contact and overall liquid volume for the three different vane cases. Instantaneous snapshots of the characteristic free surface flow and fluid-rotor contact from the CFD simulations of the three standard vane geometries are shown in Figure 12. The images shown here are from times of maximum fluid-rotor contact (minimum ALH). The fluid contact area on the side of the rotor over the 1 s of flow time following equilibration and during averaging for each vane system is plotted in Figure 13. Time zero on the plot is not the initial starting time of the simulations, but the starting time of the averaging period. The contact area plot shown here for the 4-vane geometry is generally the same as that seen previously except that the oscillation frequency and magnitude for the current simulations are more accurate relative to experimental values as noted earlier. The simulation of the curved vane geometry also evidences a periodic fluctuation in contact area; however, in this case the magnitude of the oscillation is somewhat lower than the 4-vane case and the maximum amount of contact area is roughly equal to the minimum contact area for the 4-vane geometry. There is a relatively constant low value of contact area between the fluid and the rotor side for the 8-vane geometry. The average contact area for this configuration is more than a factor of $\sim$3 less than the minimum area in the 4-vane system.

To generate a useful metric for comparison of the mixing between the different systems, it is necessary to take into

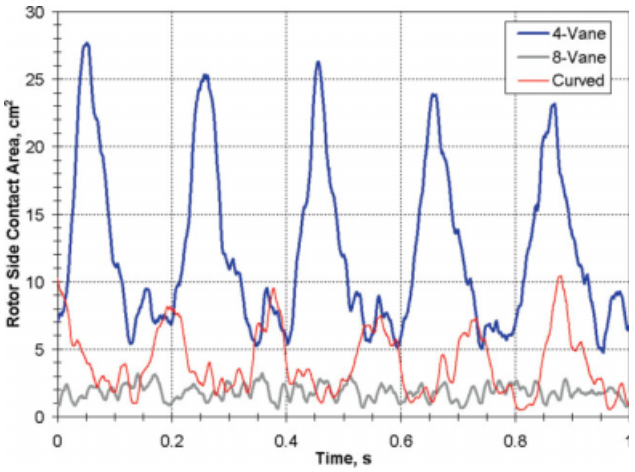

Figure 13. Plot of the fluid contact area on the side of the rotor for the three vane configurations.

Plots are for 1 s time period of flow averaging during steady-state operation. [Color figure can be viewed in the online issue, which is available at www.interscience.wiley.com.]

account not only the magnitude of the turbulence dissipation rate ε on the rotor side but also the area and duration of contact between the fluid and the rotor. One method for doing this is to define a mixing metric M_{mix} equal to the time average of the product of the spatially averaged subgrid scale dissipation rate on the rotor† $\varepsilon(t)$ (averaging over the liquid phase contact area only) and the contact area $A(t)$ according to the integral:

$$M_{\text{mix,rs}} = \frac{\rho}{t_1 - t_0} \int_{t_0}^{t_1} \varepsilon_{\text{rs}}(t) \cdot A_{\text{rs}}(t) \cdot \delta \cdot dt \tag{9}$$

for the rotor side (subscripted as rs). Multiplying by the fluid (water) density ρ and a characteristic length δ allows this mixing metric to have units of power [W]. For a constant time step, Eq. 9 becomes a simple average rather than an integral.

$$M_{\text{mix,rs}} = \rho \cdot \delta \cdot (\overline{\varepsilon_{\text{rs}}(t) \cdot A_{\text{rs}}(t)}) \tag{10}$$

While a variable time step was used in these simulations, the variation in the time step was quite small and it was found that there was <1% difference between the integral and the simple average. The simple average (and standard deviation) is used here.

A constant value of 1 mm was chosen for δ since the dissipation rate was seen to decrease nearly linearly outward from the rotor surface within this region such that the actual energy dissipation rate within this 1-mm liquid layer on the rotor side P_{mix} is proportional to M_{mix}.

$$P_{\text{mix}} \approx \beta \cdot M_{\text{mix}} \tag{11}$$

For the metric to be equivalent to the actual power dissipated in the thin liquid volume within 1 mm of the rotor surface (i.e., $\beta = 1$), an average value for the dissipation rate within this 1-mm liquid layer would be needed rather than simply taking the value at the rotor surface as was done. This is more complicated and time-consuming to do during the simulation run and therefore the mixing metric M_{mix} is useful because it uses surface-averaged quantities that are more readily calculated.

To determine the relationship between M_{mix} and P_{mix} and provide a direct comparison between these two quantities, as well as to verify that this metric of comparison did not affect the trends seen for the various vane systems, the actual power dissipated in the 1-mm liquid layer (i.e., liquid contacted areas of the rotor only) out from the rotor (both on the side and bottom) was calculated for the cases where complete data sets were saved regularly during the 1 s averaging period; this was done for all of the "standard" cases (4-vane, 8-vane, and curved). The calculation of the average power dissipated in the 1-mm liquid layer for each of these simulations was done via postprocessing of about 15 of the ~300 data sets spanning the entire 1 s of the averaging period for each geometry taking care to include extreme maximums, minimums, and mid-range values of rotor contact area. The instantaneous volumetric average of the subgrid scale dissipation rate within the computational cells inside this 1-mm liquid layer was calculated for the each of the selected data sets. For the 4-vane and curved vane geometries, it was found that the actual power dissipated in the 1-mm liquid layer was 29.9% ± 1.6% of the mixing metric M_{mix}—that is, the constant of proportionality in Eq. 11 was found to be $\beta_{\text{4-vane}} = \beta_{\text{curved}} = 0.30$. For the 8-vane geometry, the actual power dissipation P_{mix} in the 1-mm layer was a slightly smaller fraction of M_{mix} at 24.6% ± 1.9% ($\beta_{\text{8-vane}} = 0.25$). Note that these fractions were evaluated at various points over the 1 s averaging period and were found to be quite consistent over the entire range and were not themselves a function of the rotor contact area.‡

Using these values for β, the mixing metric M_{mix} is quite useful as it provides a simpler method for evaluation of the dissipation rate near the rotor during actual simulation and can be directly related to the actual power dissipation P_{mix} predicted by the simulation. The values reported throughout this section are for the actual dissipation rate P_{mix} as predicted from the mixing metric using Eq. 11 and the values reported above for β of each vane type. For the 8-vane variations, the value for the standard 8-vane case, $\beta = 0.25$, was used. Sampling for the rotor side contact area and dissipation rate was done at every 20 time steps for each simulation except for the 4-vane simulation in which the dissipation rate on the rotor was not saved during simulation but was extracted from the saved data files after the simulation was complete and therefore was only sampled for every 200 time steps. To determine the turbulence dissipation rate for just the liquid phase contacted areas of the rotor, only the areas on the rotor surface with volume fraction ϕ greater than 0.5 were included in the surface average at each

†In Fluent, values of the dissipation rate on a boundary surface such as this are interpolated from the nearest cell-center values.

‡These percentages are valid for the given rotor speed (3600 rpm) and there may be an affect on this factor of changing rotor speed. As these percentage values essentially depend on the radial gradient of the dissipation rate within the 1-mm layer, which would steepen with rotor speed, there would likely be a decrease in this ratio for a higher rotor speed. Incidentally, this may have been the reason for the smaller β value for the 8-vane geometry as it tended to have slightly higher dissipation rates very near the rotor.

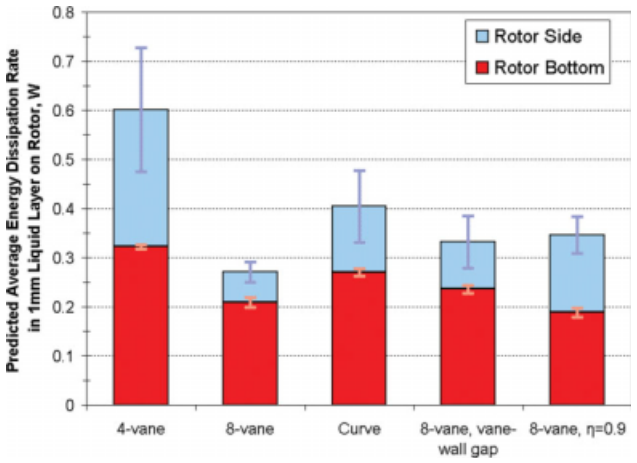

Figure 14. Comparison of the average (spatial and temporal) energy dissipation in the rotor region for the three standard vane geometries and the two 8-vane variations.

[Color figure can be viewed in the online issue, which is available at www.interscience.wiley.com.]

sampled time. This was the process for the rotor side. For the rotor bottom, the dissipation rate was also similarly sampled during the duration of the simulation, however, the liquid contact area was not. There is minimal time variation of the contact area on the rotor bottom (subscripted as rb) and therefore a single time-averaged value was used such that Eq. 10 becomes:

$$M_{\mathrm{mix,b}} = \rho \cdot \delta \cdot \overline{\varepsilon_{\mathrm{rb}}(t)} \cdot \overline{A_{\mathrm{rb}}} \tag{12}$$

Figure 14 shows a comparison of the predicted energy dissipation rate P_{mix} as calculated via the mixing metric M_{mix} using Eq. 11 (the corresponding data is also summarized in Table 4). As expected from the trends in contact area observed in Figures 8 and 13, the energy dissipation in the 4-vane geometry is significantly greater than the 8-vane or curved vane. It was observed that the average (temporal and spatial) specific turbulence dissipation rate for the total liquid-contacted area of the rotor was similar for each of the various vane systems (~600 W/kg). The average dissipation rate for the rotor bottom surface only was also similar for all systems (~500 W/kg). Values for the rate on the side of the rotor ranged somewhat from ~800 W/kg for the 4-vane to ~1400 W/kg and ~1200 W/kg for the 8-vane and curved vane geometries, respectively. While this difference in turbulence on the rotor side may seem dramatic and counter to the trends in Figure 14, the magnitude of the dissipation rate is only part of the mixing story for the free surface flow studied here—the greater the surface area over which this dissipation rate acts on the fluid, the greater the total energy imparted to the fluid, and consequently the greater the mixing. As such, the greatest difference in the energy dissipation rate as compared in Figure 14 was for the rotor side (where there is the greatest difference in contact area). Interestingly, the energy dissipated on the bottom of the rotor comprised the largest fraction of the overall dissipation for all but the 4-vane geometry. For the 8-vane geometry, where the contact area on the rotor bottom tended to be less, the overall dissipation rate in the bottom surface was lower.

For the two separate modifications to the standard 8-vane geometry, there were incremental increases in mixing relative to the standard case. It can be seen that the average energy dissipation on the rotor side and the rotor bottom were both slightly increased with the addition of the vane-wall gap. The total average energy dissipation for this modification was over 20% greater than the standard 8-vane case. The narrow gap simulation also displayed enhanced overall energy dissipation near the rotor relative to the standard case. In this case, however, there was actually a decrease in the dissipation on the rotor bottom which was more than made up for by the enhanced contact between the fluid and the side of the rotor. More details regarding the flow patterns in these two simulations is reported elsewhere.[21]

The mixing data from these different vane geometry simulations support the explanation that the fluid-rotor contact, specifically on the side of the rotor, has the largest effect on enhancing the overall operation of the mixing zone. In quantitative terms, for the given operational parameters (377 rad/s, 600 ml/min) the mixing efficiency of the 4-vane geometry (as described by the energy dissipation rate near the rotor) is approximately twice that of the 8-vane geometry and ~50% more than the curved vane geometry. Thus, it can be concluded that efforts at increasing the fluid rotor contact—which generally can be achieved through increasing the ALH—will be the most effective at increasing the mixing efficiency of the contactor mixing zone.

The other critical piece to the evaluation of mixing and overall efficiency is the equilibrium mixing zone liquid volume and the corresponding mean fluid residence time. The results from the CFD simulations are shown in Table 5. The increased liquid volume identified for the 4-vane geometry is directly correlated with the observation of greater liquid height and greater fluid-rotor contact. Even so, this greater liquid volume has a further compounding effect on the overall efficiency of operation; for liquid–liquid operation, not only would the fluids be more thoroughly mixed due to greater fluid-rotor contact, but the time that the two fluids are in contact is also longer—by more than a factor of 2.5

Table 4. Summary of the Predicted Average Energy Dissipation in the 1-mm Liquid Layer Near the Rotor for the 4, 8, and Curved Vanes as well as the Two Variation on the 8-Vane Geometry

Vane Type	Rotor Side (W)	Rotor Bottom (W)	Total (W)
4-Vane	0.279 ± 0.126	0.322 ± 0.004	0.602 ± 0.126
8-Vane	0.062 ± 0.021	0.209 ± 0.011	0.271 ± 0.023
Curved	0.135 ± 0.073	0.270 ± 0.007	0.405 ± 0.073
8-Vane, vane-wall gap	0.096 ± 0.053	0.236 ± 0.008	0.332 ± 0.054
8-Vane, $\eta = 0.9$	0.158 ± 0.037	0.188 ± 0.010	0.346 ± 0.039

Table 5. Steady-State Liquid Volume, Fluid Residence Time, and Air-Entrainment Rate for the Three Standard Vane Cases

Vane Type	Liquid Volume (ml)	Residence Time (s)	Entrained Air Flow Rate (ml/min) (% of total)
4-Vane	52.69 ± 0.70	5.27 ± 0.07	2.11 (0.35%)
8-Vane	20.59 ± 0.21	2.06 ± 0.02	17.89 (2.98%)
Curved	35.55 ± 0.39	3.55 ± 0.04	15.64 (2.61%)
8-Vane, vane-wall gap	31.80 ± 0.09	3.18 ± 0.01	–
8-Vane, $\eta = 0.9$	19.64 ± 0.24	1.96 ± 0.02	–

compared to the 8-vane and 1.5 compared to curved vane. For the 8-vane modifications, consistent with the mixing observations there was also an enhancement in the equilibrium mixing zone liquid volume and consequently the fluid residence time for the addition of the vane-wall gap. The simulation predicts that an increase of more than 50% can be achieved for these quantities relative to the base case. This 50% increase in residence time coupled with the 20% increase in mixing observed for this case combine to result in what would likely be a significant increase in operational efficiency for this minor modification. On the other hand, the increase in liquid height for the narrow gap case is counteracted by the decrease in the annular flow area resulting in an equilibrium liquid volume slightly less than the standard case.

Another indicator of the potential operational behavior of the various contactor housing geometries is the amount of air entrainment. Various researchers identify air entrainment as having a detrimental effect on extraction efficiency.[23,24] Because of the poor fluid-rotor contact and relatively strong forcing of the fluid into the rotor for the 8-vane and curved vane geometries, there is significant bubble entrainment in these configurations as observed by the pumping of air into the rotor (last column of Table 5). In general, all of these indicators point toward a ranking of the relative mixing zone operational efficiency for the three different vane types at the given operational settings examined here according to: 4-vane > curved vane > 8-vane. Additionally, this set of simulations demonstrates the effect that a couple of minor variations to the standard 8-vane geometry can have on the flow in the mixing zone. An increase in mixing for the same overall liquid volume was observed for the narrow annular gap geometry. Perhaps more importantly, it was demonstrated that a very simple modification to the standard 8-vane geometry—the addition of a vane-wall gap—could result in a 22% increase in mixing efficiency and a 54% increase in fluid residence time relative to the standard 8-vane case.[§] While this was not explored, the ''trade-off'' for increased mixing through the addition of the vane-wall gap would likely be a decrease in the maximum throughput of the mixing zone. However, contactors are generally designed such that the maximum throughput is limited by the amount of phase separation that can be achieved for the given separation height[25] so this decrease may not be an issue.

Conclusions

The research presented in this article has applied a range of experimental measurements and observations to the analysis of the flow in the mixing zone of the annular centrifugal contactor. The computational methodology that was demonstrated in the previous work[4] has been further validated and applied to perform a detailed analysis and comparison of the flow and mixing for several possible housing vane configurations. In general, it has been seen that the housing vane geometry has a significant impact on the overall flow patterns, liquid height and liquid volume, fluid-rotor contact, and energy dissipation rate in the rotor region.

In terms of mixing effectiveness, two main effects were compared here, namely, the dissipation rate and the fluid residence time—which translate into greater mass transfer area and greater mass transfer time, respectively. Without the addition of detailed coupled chemical and extraction kinetics to the modeling, it is not possible to evaluate the optimum balance of surface area, contact time, and throughput. Certainly, the optimum balance would depend on the characteristics of the specific process being used within the contactor units. Further development of the modeling scheme to include these factors would be a useful subsequent stage in the centrifugal contactor simulation effort. Even so, the present comparison has shown both qualitatively and quantitatively that the mixing vane geometry has a clear impact on the overall effectiveness of the mixing zone. The conclusions obtained from the simulations were compared with a variety of experimental observations and found to have generally good predictive accuracy for the flow of water in the mixing zone. From this, it is anticipated that the experimental analysis and modeling scheme set forth here can aid in the proper selection of contactor geometry as well as lend insight into ways to improve the design of existing contactor units with minimal modification.

In particular, from this comparison it can be concluded that among the given configurations, one might select the 4-vane geometry for better low flow rate operation as it maintains a predictable liquid volume with greater fluid-rotor contact; however, at high flow rates ($\geq$1000 ml/min) the liquid level is such that nearly the entire mixing zone is filled and there is the risk of overflow into the lower phase collector ring and phase contamination. This marks a practical upper limit for this geometry. While high flow rates were not simulated, it has generally been observed that adequate operation can be achieved with either the curved vanes or 8-vanes at high flow rates. For some processes and phase pairs, there may be issues with overmixing and emulsification. In such cases, this type of analysis could certainly aid in selecting an appropriate geometry and targeting experiments for improving operation for the flow conditions specified by the process. It has also been demonstrated that a noticeable improvement, both in terms of mixing and residence time, can be achieved through the simple addition to the standard 8-vane geometry of a vane-wall gap with a width equal to half the annular gap ($0.5\Delta r$).

[§]Although it was not explored here, the vane-wall gap may also have the additional benefit in that it removes a potential area of accumulation for particulates (i.e., the region where the vane meets the wall).

Acknowledgments

Kent Wardle would like to thank Argonne National Laboratory's Chemical Sciences and Engineering Division for partial support of this work. This work was also partially supported by the National Center for Supercomputing Applications under TG-ECS070009 and utilized the Tungsten Cluster. This research was performed under appointment to the U.S. Department of Energy Nuclear Engineering and Health Physics Fellowship Program sponsored by the U.S. Department of Energy's Office of Nuclear Energy, Science, and Technology.

Literature Cited

1. Bernstein G, Grosvenor D, Lenc J, Levitz N. Development and performance of a high-speed annular centrifugal contactor. Technical Report ANL-7969. Argonne National Laboratory, Argonne, 1973.
2. Yarbro SL, Schreiber SB. Using process intensification in the actinide processing industry. *J Chem Technol Biotechnol*. 2003;78:254–259.
3. Leonard R, Regalbuto M, Aase S, Arafat H, Falkenberg J. Hydraulic performance of a 5-cm contactor for caustic-side solvent extraction. Technical Report ANL-02/18. Argonne National Laboratory, Argonne, 2002.
4. Wardle KE, Allen TR, Anderson MH, Swaney RE. Free surface flow in the mixing zone of an annular centrifugal contactor. *AIChE J*. 2008;54:74–85.
5. Birdwell JF, Anderson KK. Evaluation of 5-cm centrifugal contactor hydraulic and mass transfer performance for caustic-side solvent extraction of cesium. Technical Report ORNL/TM-2001/137. Oak Ridge National Laboratory, Oak Ridge, 2001.
6. Birdwell JF, Anderson KK. Evaluation of mass transfer performance for caustic-side solvent extraction of cesium in a conventional 5-cm centrifugal contactor. Technical Report ORNL/TM-2001/278. Oak Ridge National Laboratory, Oak Ridge, 2002.
7. Law J, Tillotson R, Todd T. Evaluation of the hydraulic performance and mass transfer efficiency of the CSSX process with the optimized solvent in a single stage of 5.5-cm diameter centrifugal contactor. Technical Report INEEL/EXT-02-01106. Idaho National Engineering and Environmental Laboratory, Idaho, 2002.
8. Law J, Meikrantz D, Garn T, Mann N, Herbst S, Todd T. The testing of commercially available engineering- and plant-scale annular centrifugal contactors for the processing of spent nuclear fuel. Technical Report INL/CON-06-11498. Idaho National Laboratory, Idaho, 2006.
9. Bonnessen PV, Delmau LH, Moyer BA, Leonard RA. A robust alkaline-side CSEX solvent suitable for removing cesium from Savannah River tank waste. *Solvent Extr Ion Exch*. 2000;18:1079–1107.
10. Zlokarnik M. *Stirring: Theory and Practice*. Weinheim: Wiley-VCH, 2001.
11. Hinze J. Fundamentals of the hydrodynamic mechanism of splitting dispersion processes. *AIChE J*. 1955;1:289.
12. Andersson R, Andersson B. On the breakup of fluid particles in turbulent flows. *AIChE J*. 2006;52:2020.
13. Haas P. Turbulent dispersion results from gel-sphere processes and application to centrifugal contactors. Technical Report ORNL/TM-9950. Oak Ridge National Laboratory, Oak Ridge, 1986.
14. Haas P. Turbulent dispersion of aqueous drops in organic liquids. *AIChE J*. 1987;33:987.
15. Davies J. Drop size of emulsions related to turbulent energy dissipation rates. *Chem Eng Sci*. 1985;40:839–842.
16. Zhou G, Kresta SM. Correlation of mean drop size and minimum drop size with the turbulence energy dissipation and the flow in an agitated tank. *Chem Eng Sci*. 1998;53:2063–2079.
17. Zhou G, Kresta S. Impact of tank geometry on the maximum turbulence energy dissipation rate for impellers. *AIChE J*. 1996;42:2476.
18. Villermaux J. The role of energy dissipation in contacting and mixing devices. *Chem Eng Technol*. 1988;11:276.
19. Lemenand T, Dupont P, Velle DD. Turbulent mixing of two immiscible fluids. *J Fluids Eng*. 2005;127:1132.
20. Kim WW, Menon S. Application of the localized dynamic subgrid-scale model to turbulent wall-bounded flows. In: *35th AIAA Aerospace Sciences Meeting and Exhibit,* Reno, NV, January 6–9, 1997.
21. Wardle KE. Computational and experimental analysis of the flow in an annular centrifugal contactor. Ph.D. Dissertation. University of Wisconsin-Madison, Madison, 2008.
22. Sheldon BV, Flim WD, Mendoza G, Macaluso LL. Method of making an easily disassembled rotor assembly for a centrifugal separator. U.S. Patent 6,363,611 B1, 2002.
23. Jubin RT, Randolph JD. Centrifugal contactor with liquid mixing and flow control vanes and method of mixing liquids of different phases. U.S. Patent 5,024,627, 1991.
24. Rivalier P, Duhamet J, Gandi F. Annular centrifugal extractor with embedded stirring rotor. U.S. Patent 7,134,991 B2, 2006.
25. Leonard R, Bernstein G, Pelto R, Ziegler A. Liquid-liquid dispersion in turbulent Couette flow. *AIChE J*. 1981;27:495.

Manuscript received Jun. 19, 2008, and revision received Jan. 7, 2009.